Science Advances
AAAS

Supplementary Materials for

Periplasmic biomineralization for semi-artificial photosynthesis

Yiliang Lin *et al.*

Corresponding author: Bozhi Tian, btian@uchicago.edu; Xiang Gao, gaoxiang@siat.ac.cn

Sci. Adv. **9**, eadg5858 (2023)
DOI: 10.1126/sciadv.adg5858

This PDF file includes:

Table S1. Summary of the key discovery, key information, methodology and data in this work.

Key Discoveries	Key Information	Methodology	Figure Panels
Formation of semiconductor nanoparticles within the microbes	Semiconductor nanoparticles formation in microbe with materials characterization	• STEM • SEM • EDS • Fluorescent microscope • XRD	Figs. 1D-1E Figs. S1-S3 Figs. 3E-3G Figs. S11-13
	Removal of heavy metal with together semiconductor formation	• Flask culture	Figs. 2A-2B Fig. S4
	Understand the semiconductor nanoparticles formation with biological characterizations	• Transcriptomic • Genetic knockouts • H_2S production measurement	Figs. 4A-4B Figs. S15-S23
Biohybrid formation with periplasmic bio-interface for semi-artificial photosynthesis	Biohybrid formation characterization	• STEM • 3D X-ray fluorescence tomography	Figs. 2C-2F Figs. S6-S8
	Mineralization at periplasm	• STEM • EDS	Figs. 3A-3D Figs. S9-S10
	Semi-artificial photosynthesis	• Transcriptomic • Bioproduction	Figs. 5A-5E Figs. S28-S31
Extended applications	Multi-metals removal	• TEM • STEM • EDS • XRD	Figs. 4C-4G Figs. S11-S13 Figs. S24-S27
	Flow-based reactor	• Flow-based reactor	Figs. 4H-4I Fig. S28

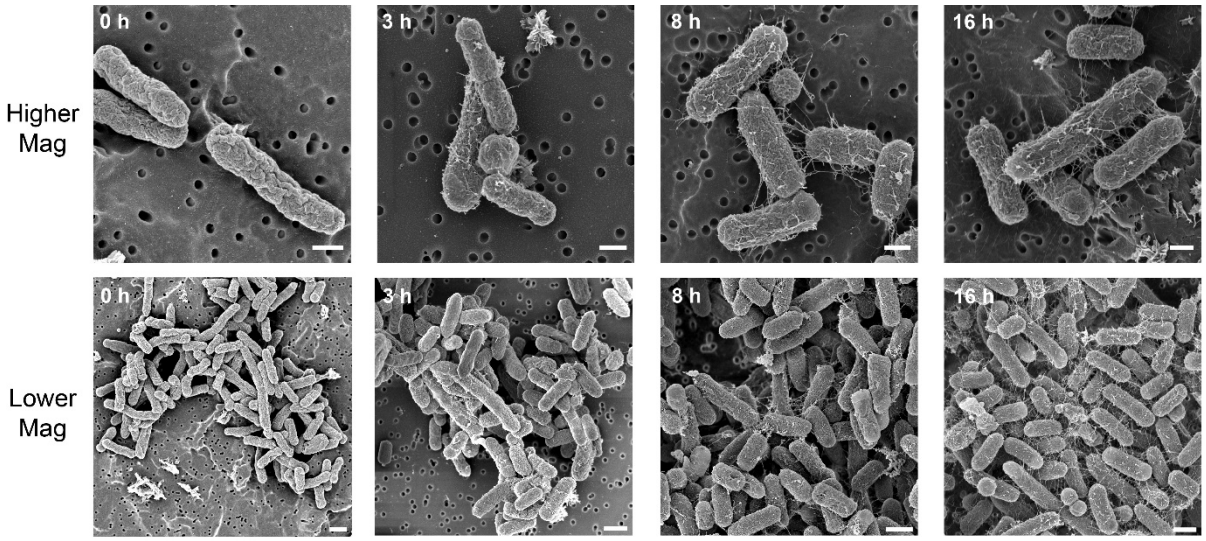

Fig. S1. SEM images of bacteria incubated in Cd^{2+}/Cys-containing medium at 0 h, 3 h, 8 h, and 16 h. SEM images show the growth of fimbriae. Fimbriae begin to form after ~ 3 h and continue to grow over time. Scale bar, 500 nm (upper panels) and 1 μm (lower panels).

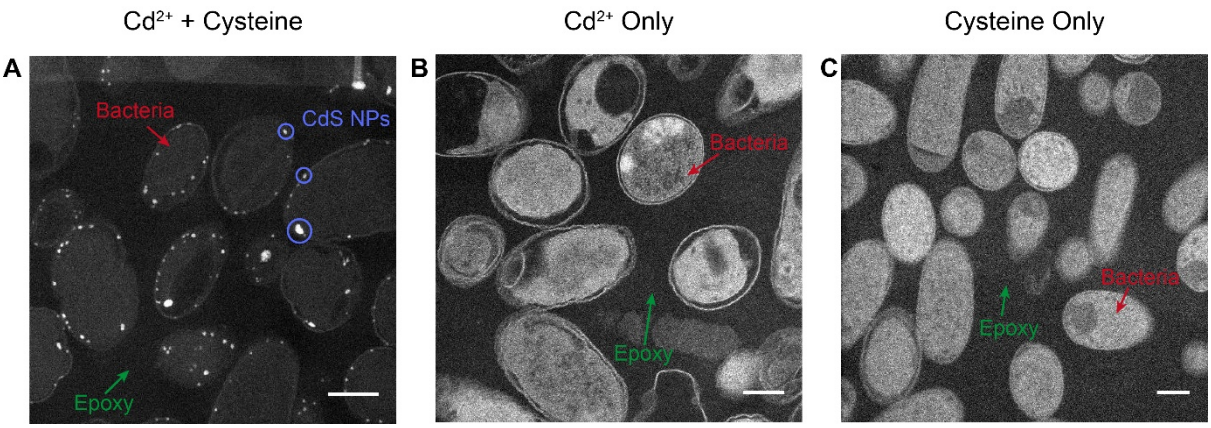

Fig. S2. Cross-sectional STEM images of *E. coil* under different culture conditions show that both Cd^{2+} and cysteine are necessary for nanocluster biomineralization. Cd^{2+} only and cysteine only culture conditions will not induce biomineralization. Figures S2A and S2C&c have different backgrounds due to the different contrast with/without CdS nanoparticle formation. The CdS nanoparticles will have a defined structure and shape as bright spots in the STEM image, as shown in Fig. S2A. Since the bacterial cells were stained with uranyl acetate, they appear whiter in Fig.S2B&C due to STEM HAADF Z-contrast imaging. Scale bar, 500 nm.

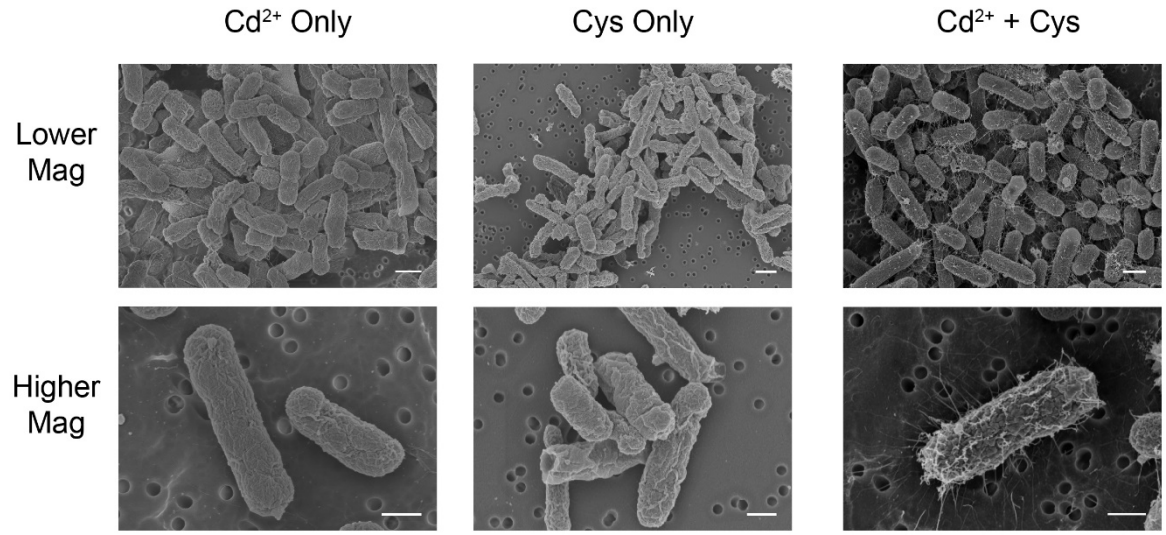

Fig. S3. SEM images of *E. coil* under different culture conditions show that both Cd^{2+} and cysteine are necessary for the growth of the fimbriae. Cd^{2+} only and cysteine only culture conditions will not stimulate the growth of the fimbriae. Scale bar, 1 μm for lower magnifications and 500 nm for higher magnifications.

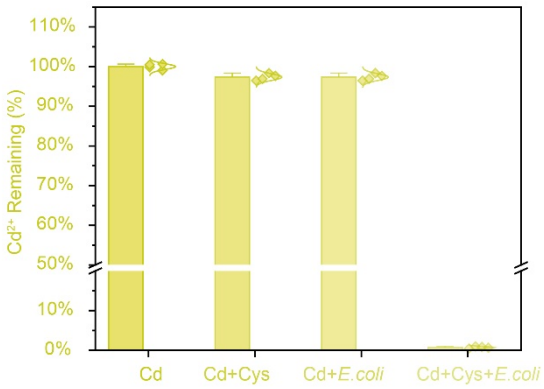

Fig. S4. The *E. coli* flask culture can remove heavy metals at very high efficacy with the presence of cysteine. Plots of the remaining Cd^{2+}metal ions (percentages) in the medium after flask culture treatment under varying culture conditions indicate that with cysteine and *E. coli*, the flask culture can achieve high removal efficiency.

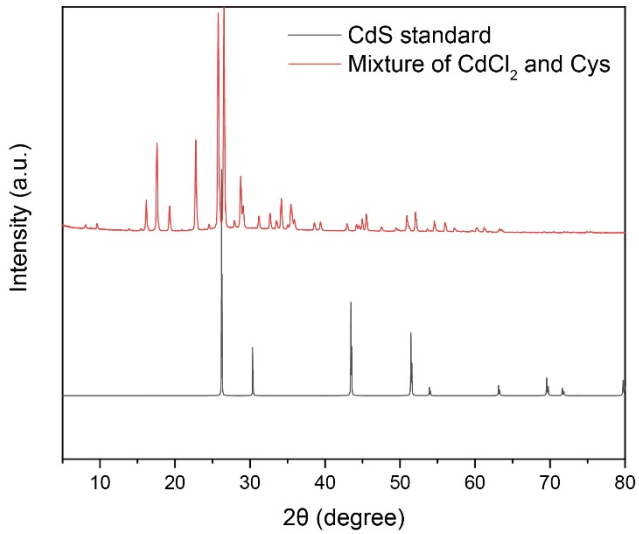

Fig. S5. Mixing Cd^{2+} and cysteine can't form CdS, as confirmed by XRD data.

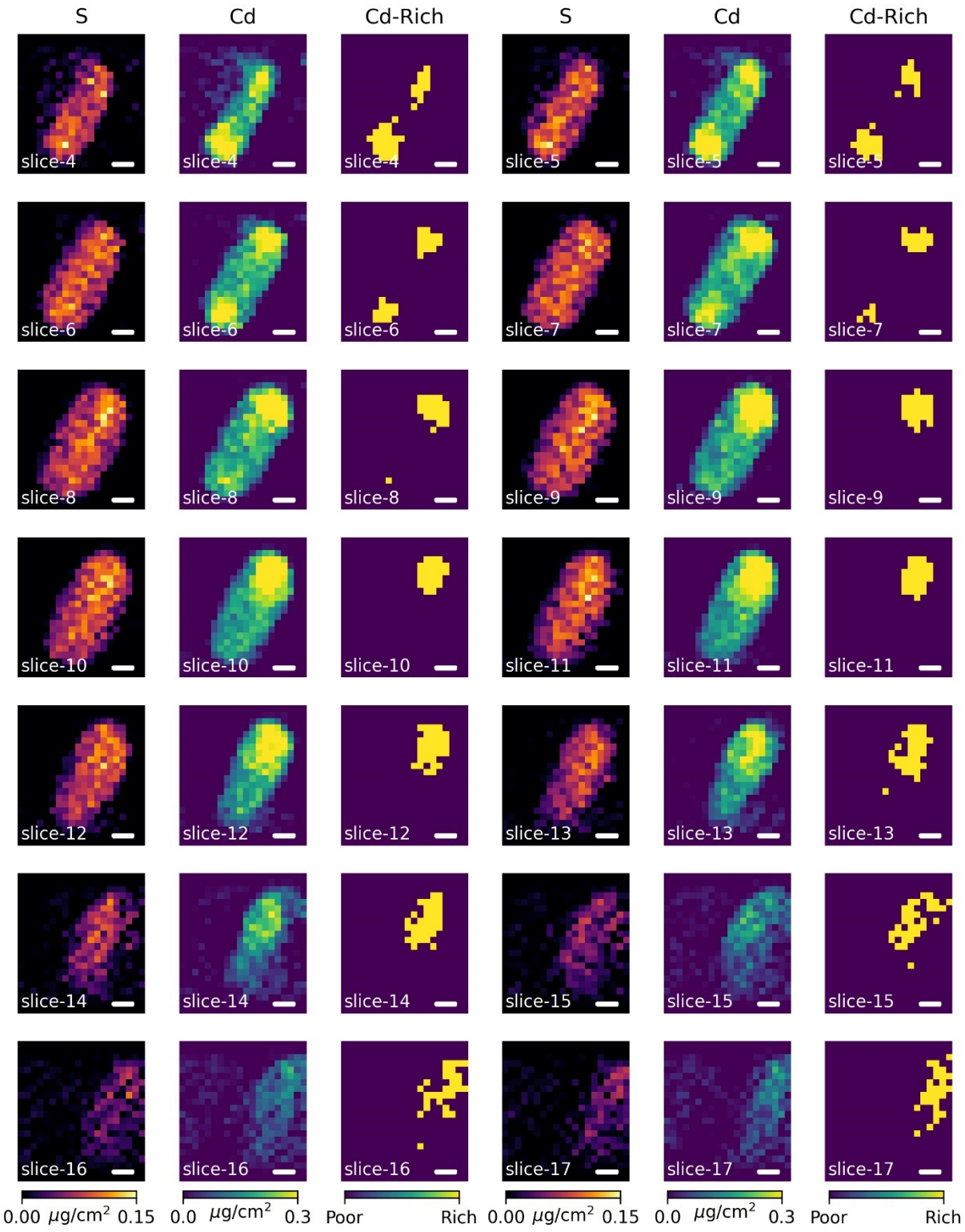

Fig. S6. Spatial distribution of S and Cd in virtual cross-sectional slices after 3D tomography reconstruction. Cd-rich regions are identified when the pixel intensity is beyond 2 times of standard deviation from the mean in each virtual slice. Scale bar, 200 nm.

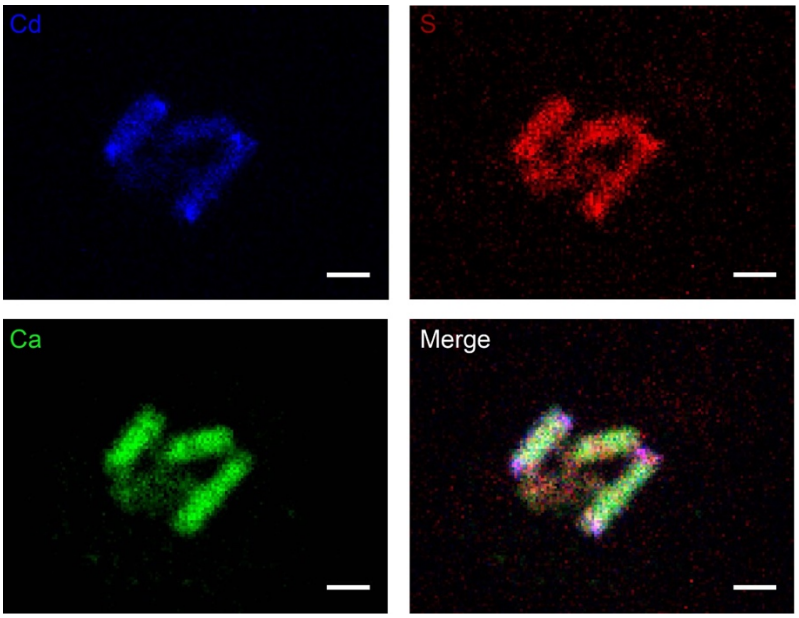

Fig. S7. X-ray fluorescence imaging of bacterial cells shows the distribution of the elements. The images confirm the chemical enrichment of cadmium and sulfur on the bacteria. Scale bar, 1 μm.

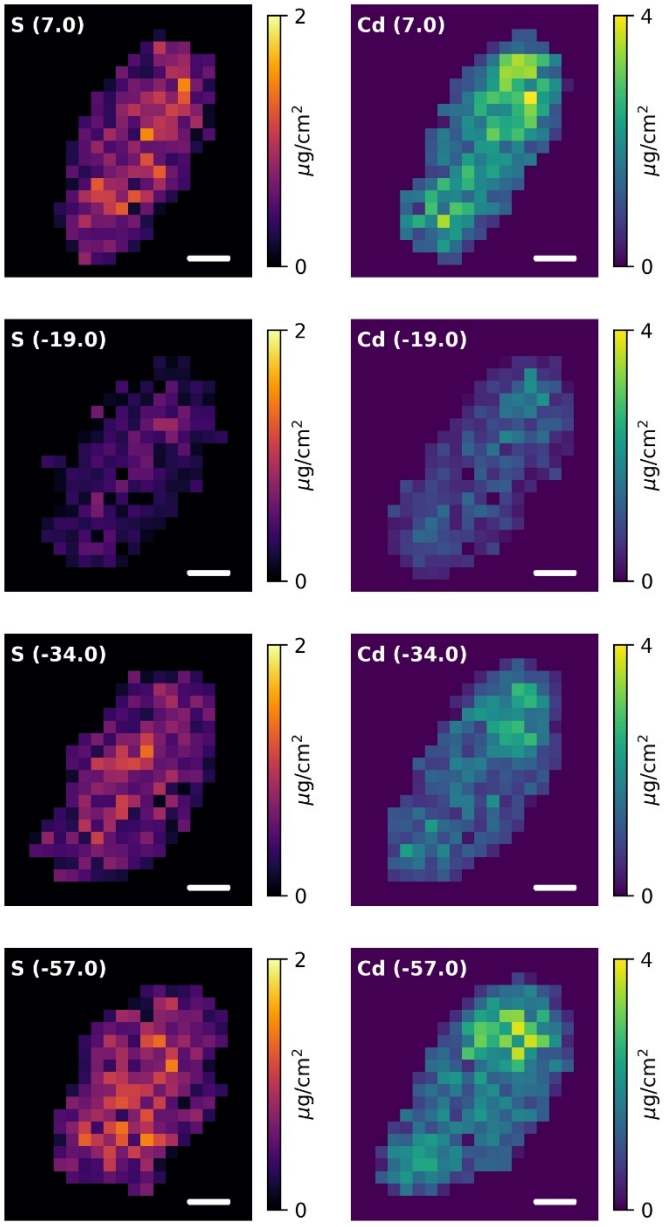

Fig. S8. **Selective X-ray fluorescence maps showing S and Cd elemental distribution within an *E. coli* cell at various sample rotations over a tomography scan.** The bacterial cell in each projection was isolated from the background by performing k-means clustering analysis. The angle of rotation is denoted on the top left label within the parenthesis. Scale bar, 200 nm.

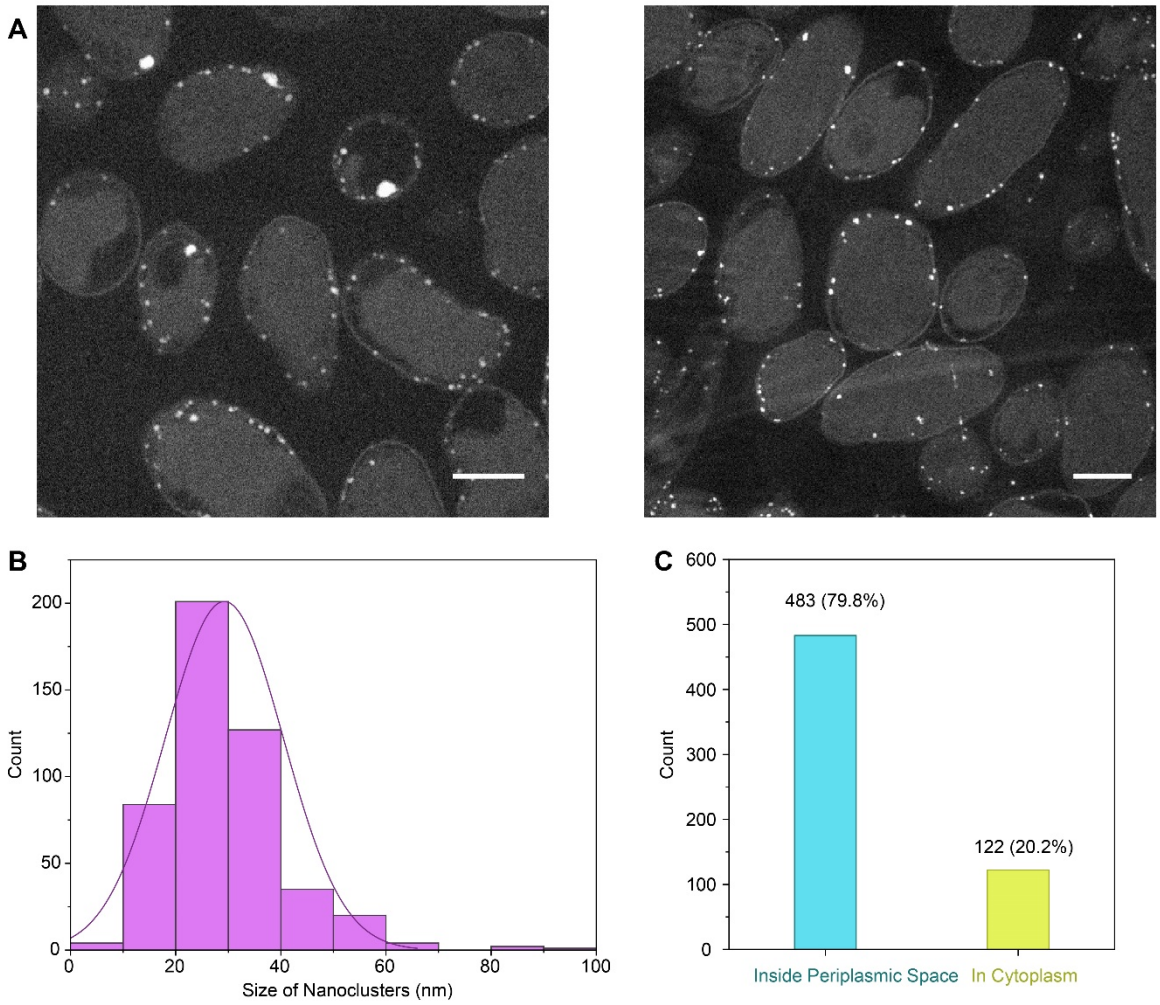

Fig. S9. The biomineralized nanoclusters are mainly located in the periplasmic space. A) Cross-sectional STEM images showed most of the nanoclusters are located in the periplasmic space. Scale bar, 500 nm. **B**) The CdS nanoclusters in the bacterial cells have an average size of 29.3 nm based on cross-sectional STEM images. The size distribution corresponds to over 400 nanoclusters. **C**) Statistical analysis further confirmed that 483 out of 605 particles (79.8%) were located between the inner and outer membranes with clear boundaries. It is noteworthy that we only defined those particles as being within the periplasmic space. However, for *E. coli*, the periplasmic space could occupy up to 40% of the cell volume. Therefore, the percentage within periplasmic space might be underestimated.

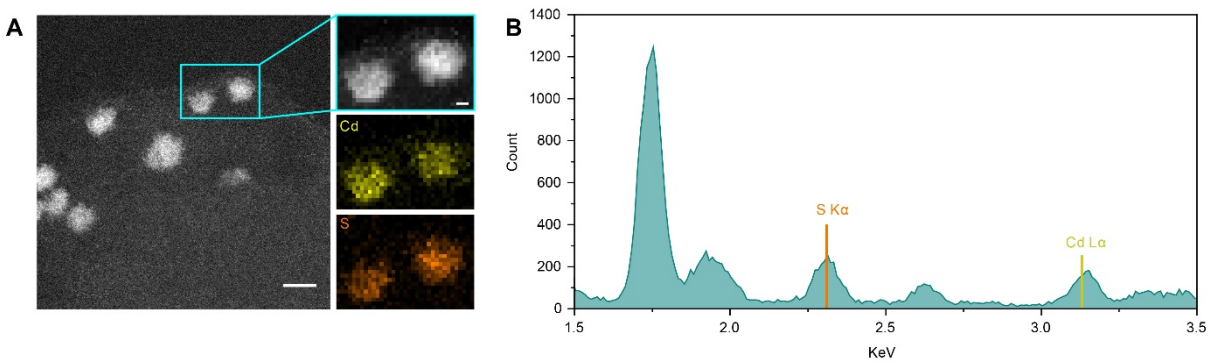

Fig. S10. Elemental mapping confirmed the precipitated nanoclusters are composed of Cd and S elements. A) A STEM image of a representative area on the bacteria with precipitated aggregates. Scale bars, 50 nm and 10 nm. **B**) Energy-dispersive X-ray spectroscopy (EDS) in STEM confirms the existence of Cd and S.

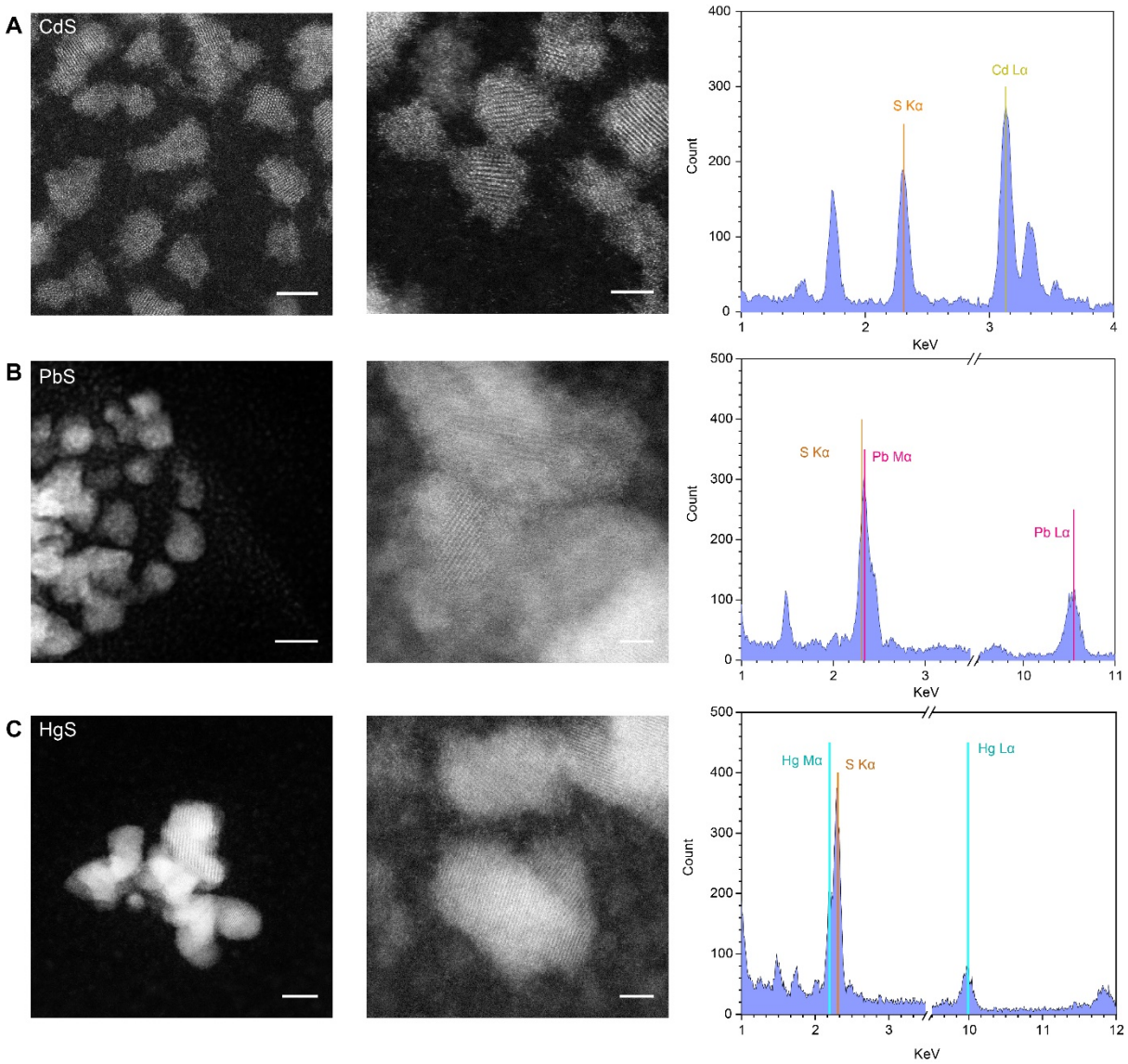

Fig. S11. High-resolution STEM images and corresponding EDS spectrum of the CdS, PbS and HgS nanoparticles. A) High-resolution STEM images of CdS nanoparticles and the corresponding EDS spectra show the co-existence of Cd and S elements. Scale bars, 5 nm, and 3 nm. **B**) High-resolution STEM images of PbS nanoparticles and the corresponding EDS spectra show the co-existence of Pb and S elements. Scale bar, 20 nm, and 3 nm. **C**) High-resolution STEM images of HgS nanoparticles and the corresponding EDS spectra show the co-existence of Hg and S elements. Scale bars, 10 nm, and 3 nm.

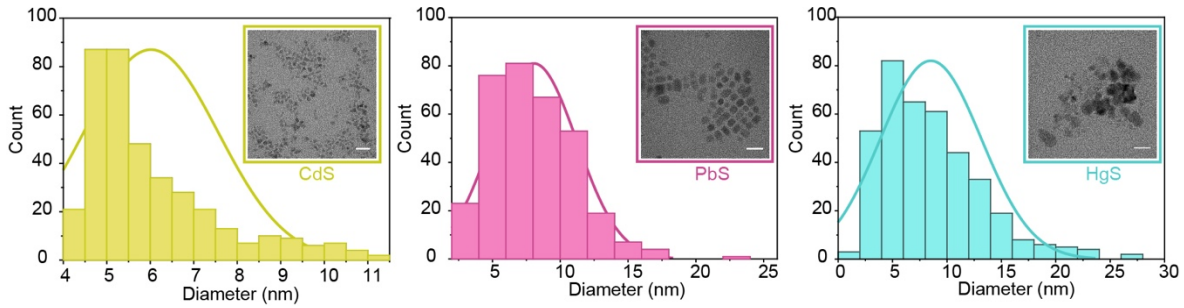

Fig. S12. Histograms showing the diameter distribution of CdS, PbS and HgS nanoparticles after extraction from the biohybrid. The CdS, PbS, and HgS nanoparticles have diameters of 6.02 ± 1.55 nm, 8.06 ± 3.15 nm, and 8.52 ± 4.65 nm, respectively (n>300). The corresponding inset TEM images show the morphology of the small nanoparticles. Scale bar, 20 nm.

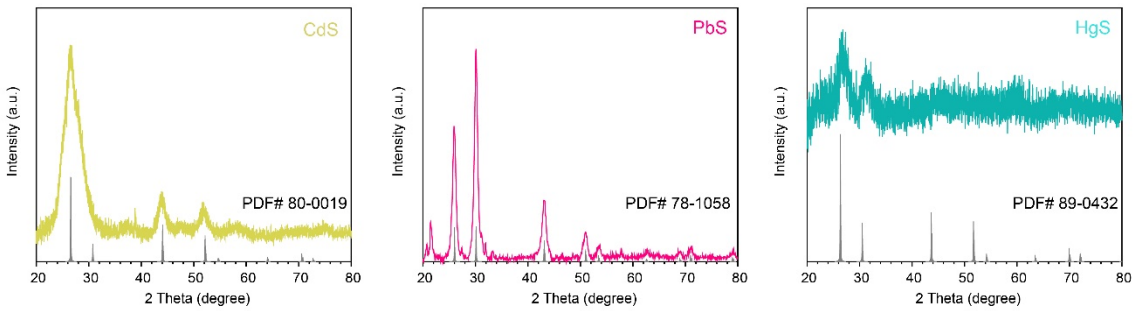

Fig. S13. XRD confirms the crystal structures of the CdS, PbS, and HgS nanoparticles after extraction from the biohybrid. The measured XRD signals match well with those grey peaks come from standard PDF files.

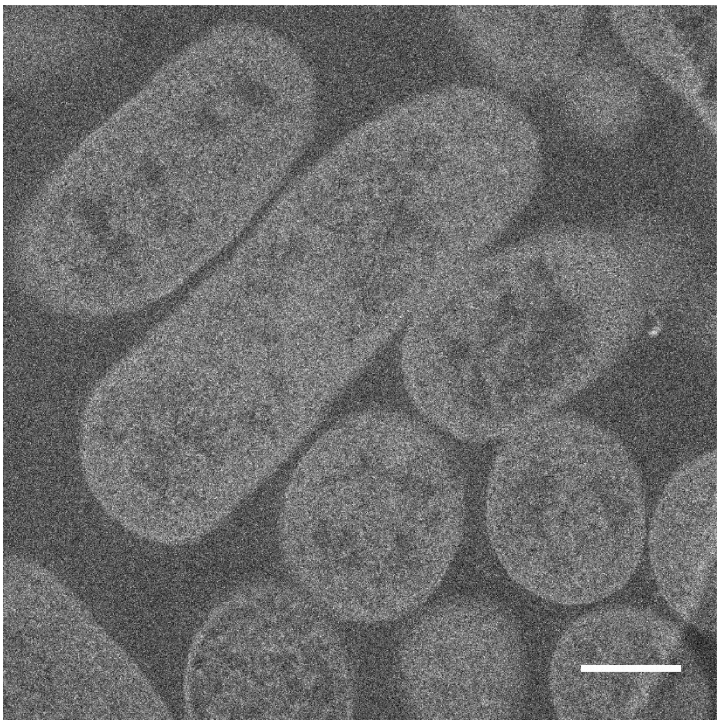

Fig. S14. Cross-sectional TEM images of intact bacterial cells but metabolically inactive (dead bacterial cells) cannot produce CdS nanoclusters. The representative TEM image of dead bacteria shows no formation of CdS nanoclusters, in contrast to those of living bacteria with nanoparticles forming in the periplasmic space (Fig. S9). The benchmark experiment confirms that metabolic activity is required for semiconductor biomineralization. Scale bar, 500 nm.

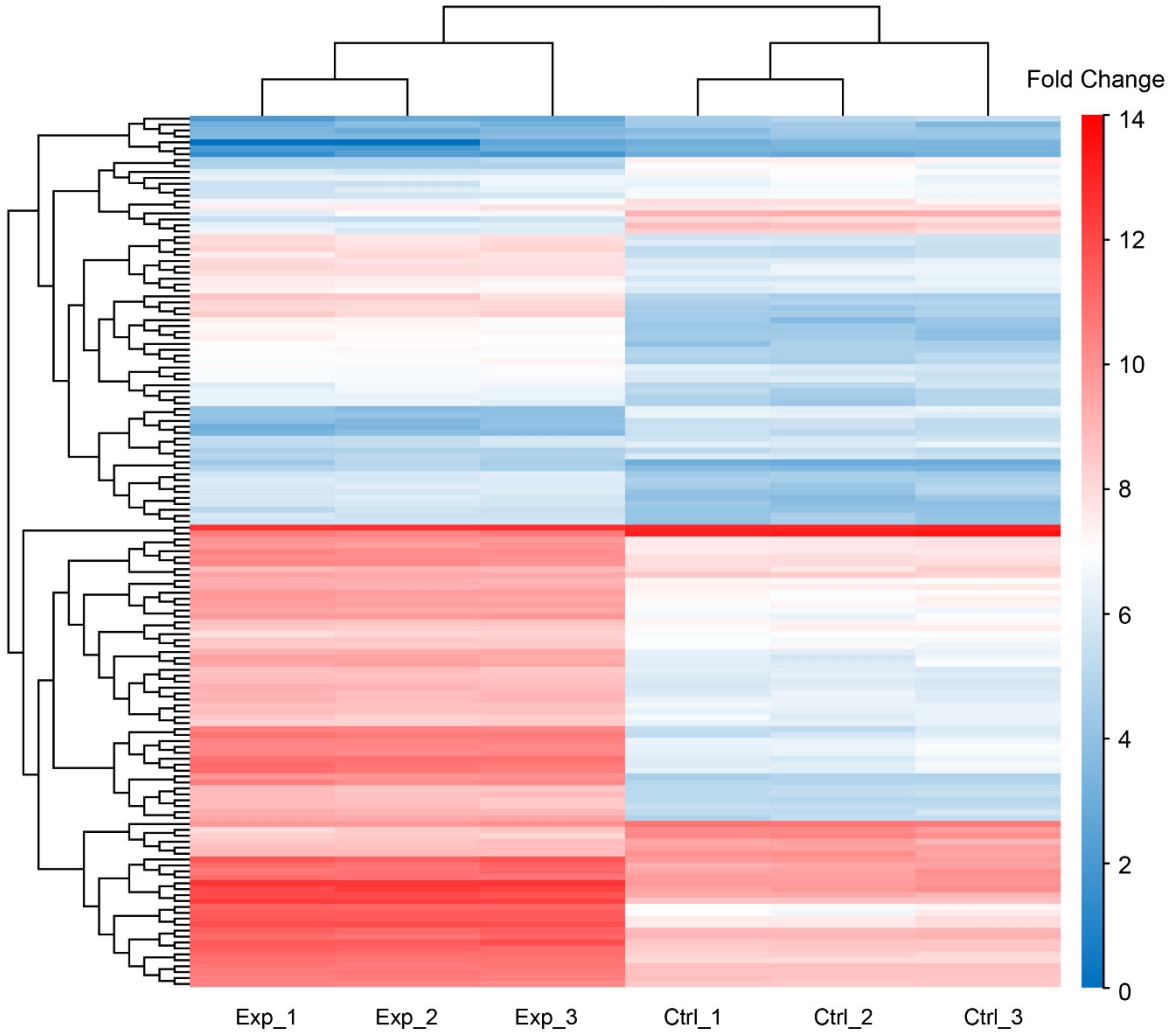

Fig. S15. Hierarchical clustering analysis of RNA-Seq differential expression data in three individual control group samples treated with Cd^{2+} only and experimental group samples treated with Cd^{2+} and cysteine.

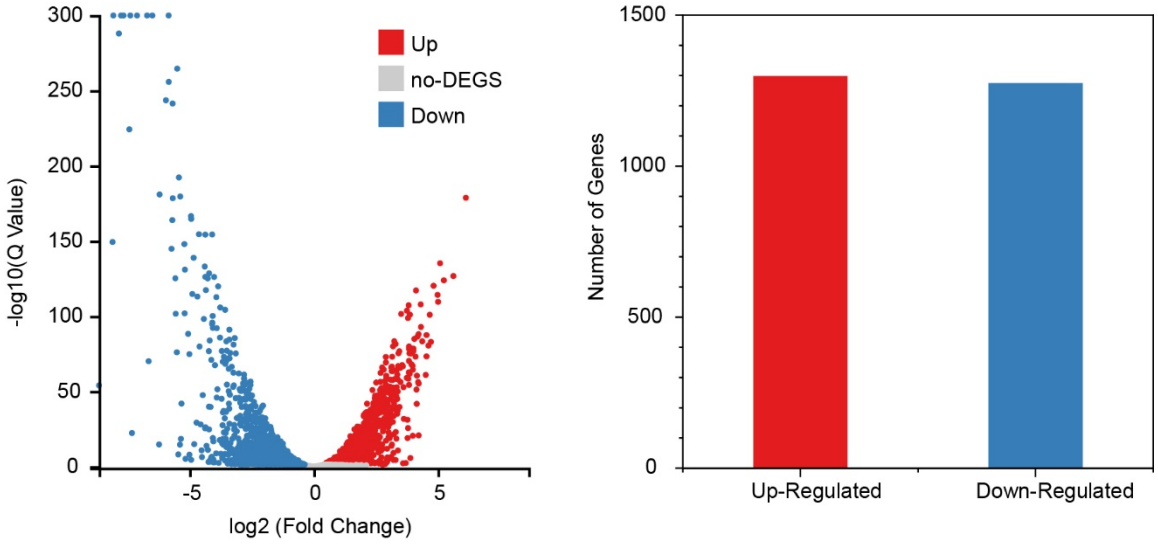

Fig. S16. Identification of differentially expressed genes in RNA-Seq data. Volcano plot showing the statistical significance versus magnitude of fold change in our RNA sequencing data. Compared to the control group treated with Cd^{2+} only, the experimental group treated with Cd^{2+} and cysteine has 1298 up-regulated genes and 1275 down-regulated genes.

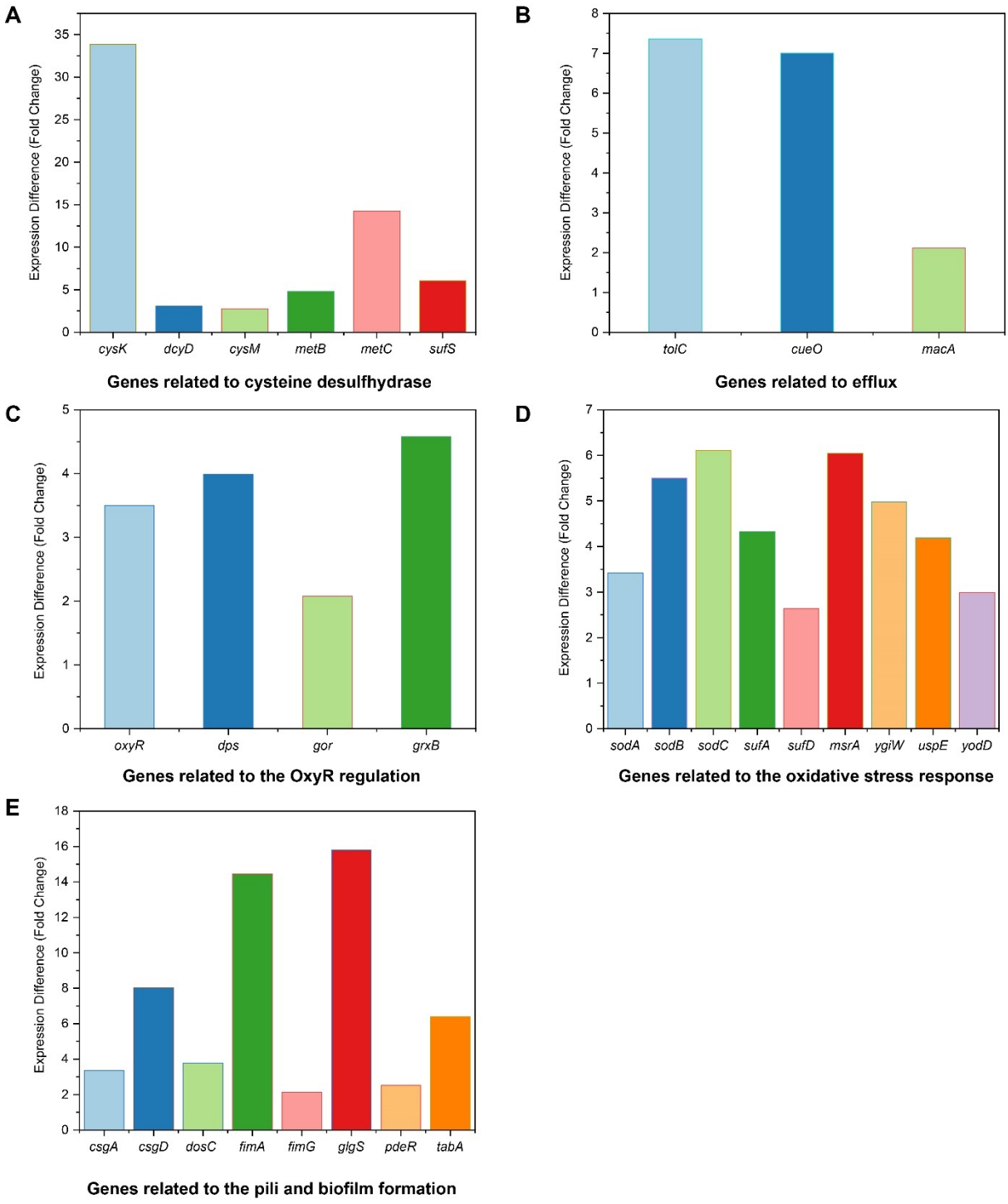

Fig. S17. Up-regulation of different genes related to the biomineralization process. A) Multiple cysteine desulfhydrase genes, including *cysK* (+33.85), *dcyD* (+3.08), *cysM* (+2.76), *metB* (+4.81), *metC* (+14.23), *sufS* (+6.05), were up-regulated in Cd^{2+} and cysteine treated *E. coli* cells compared to those treated with Cd^{2+} only. **B**) Multiple efflux-related genes, including *tolC* (+7.36), *cueO* (+7.00), and *macA* (+2.11), were up-regulated in Cd^{2+} and cysteine treated *E. coli* cells compared to those treated with Cd^{2+} only, indicating the efflux of Cd^{2+} into the periplasmic space. **C**) Multiple *OxyR*-related genes, including *oxyR* (+3.50), *dps* (+3.99), *gor* (+2.08), *grxB* (+4.58), were up-regulated in Cd^{2+} and cysteine treated *E. coli* cells compared to those treated with Cd^{2+} only, suggesting that the synthesized CdS nanoparticles contribute to the induced oxidative stress in the *E.coli* cells. **D**) Multiple oxidative stress

response-related genes, including *sodA* (+3.42), *sodB* (+5.50), *sodC* (+6.11), *sufA* (+4.33), *sufD* (+2.64), *msrA* (+6.05), *ygiW* (+4.98), *uspE* (+4.19), and *yodD* (+2.99), were up-regulated in Cd^{2+} and cysteine treated *E. coli* cells compared to those treated with Cd^{2+} only, suggesting the *E. coli* cells were under increased oxidative stress during the nanoparticle and fimbriae formation. **E**) Multiple oxidative stress response-related genes, including *csgA* (+3.36), *csgD* (+8.02), *dosC* (+3.78), *fimA* (+14.46), *fimG* (+2.13), *glgS* (+15.79), and *tabA* (+6.40), were up-regulated in Cd^{2+} and cysteine treated *E. coli* cells compared to those treated with Cd^{2+} only.

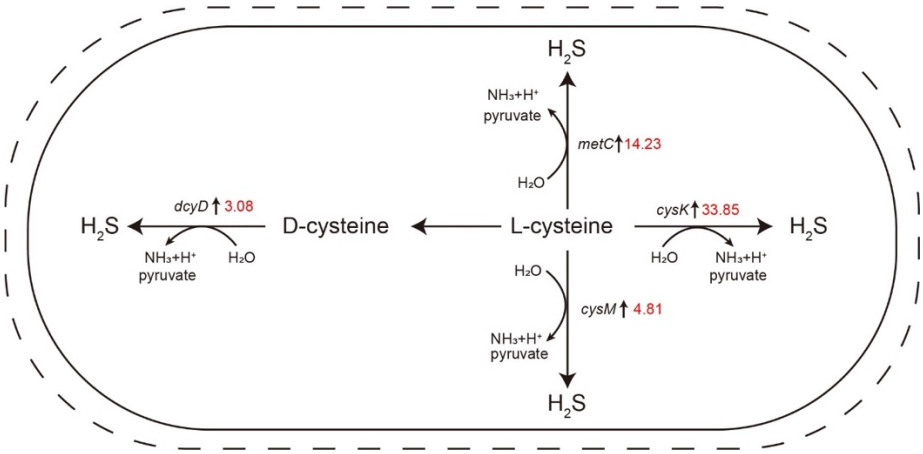

Fig. S18. Multiple biological pathways to metabolize cysteine into H_2S. Cysteine could be metabolized through different biological pathways, and we discovered the up-regulation of several genes in Cd^{2+} and cysteine-treated samples that are directedly related to H_2S synthesis, including *cysK, dcyD, cysM,* and *metC*, in comparison with Cd^{2+} treated samples.

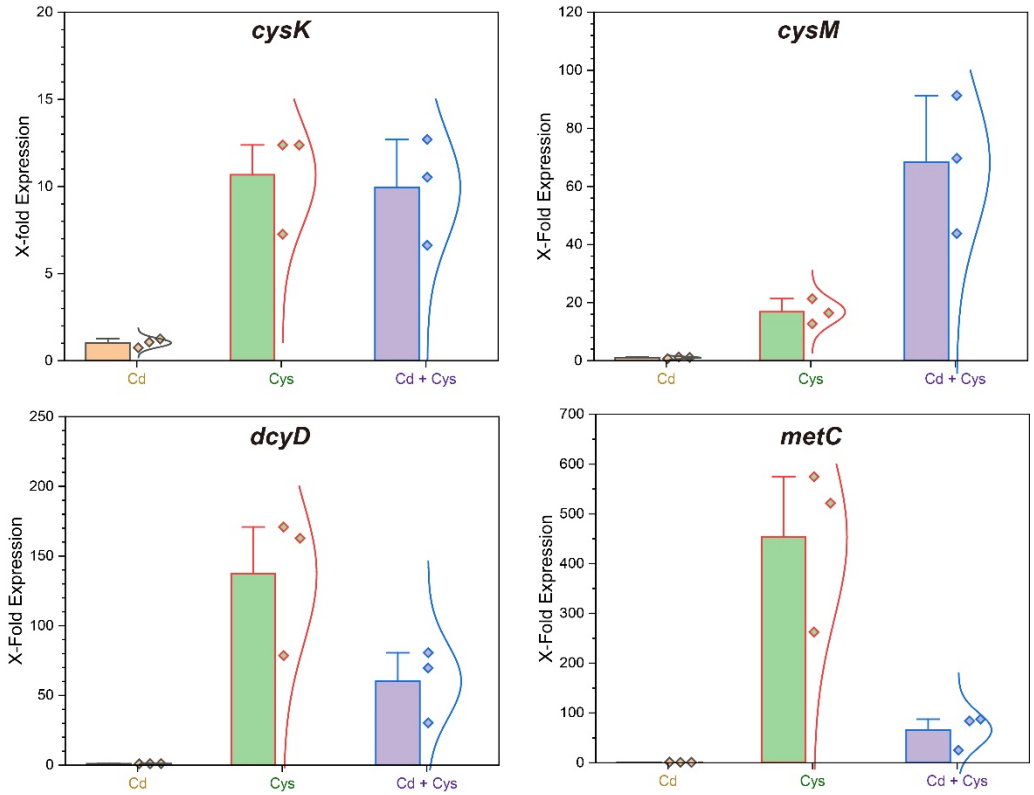

Fig. S19. The addition of cysteine can enhance genes expression related to H_2S production and gene, such as *cysM* can be further up regulated with the presence of Cd^{2+}.

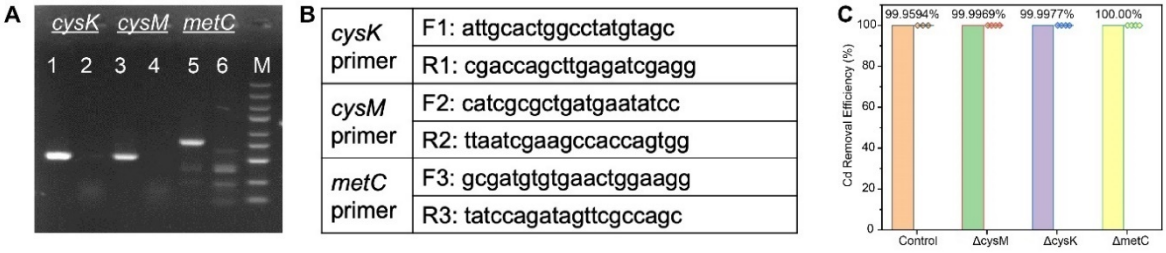

Fig. S20. The mutants' experiments suggest the functional redundancy of multiple genes involved in H_2S synthesis. A). The mutants were verified by PCR; 1, *cysK* mutant; 3, *cysM* mutant; 5, *metC* mutant; 2, 4, 6, the wild type *E. coli* strain. B) The PCR primers used in A. C) All the mutants can show very high heavy metal removal efficiency, similar to the control sample of wild type *E . coli* strain.

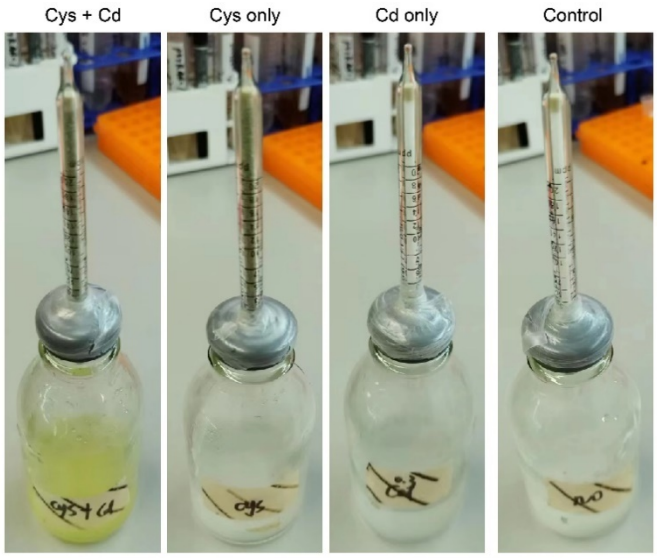

Fig. S21. Without the addition of cysteine, *E. coli* culture can't produce detectable H_2S with lead acetate hydrogen sulfide indicator strips

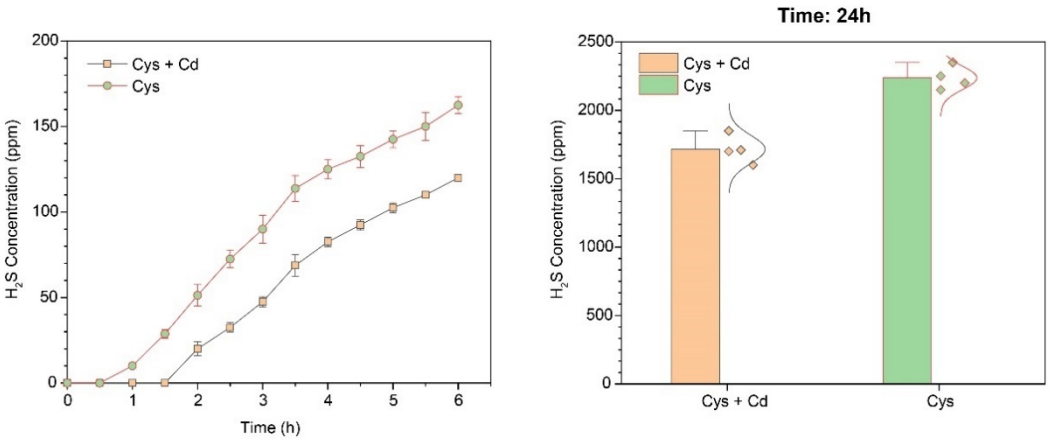

Fig. S22. The group with both cysteine and Cd^{2+} produced less detectable H_2S over 24 h process. This indicates some synthesized H_2S might be used for the biomineralization of Cd^{2+} within the bacterial cells.

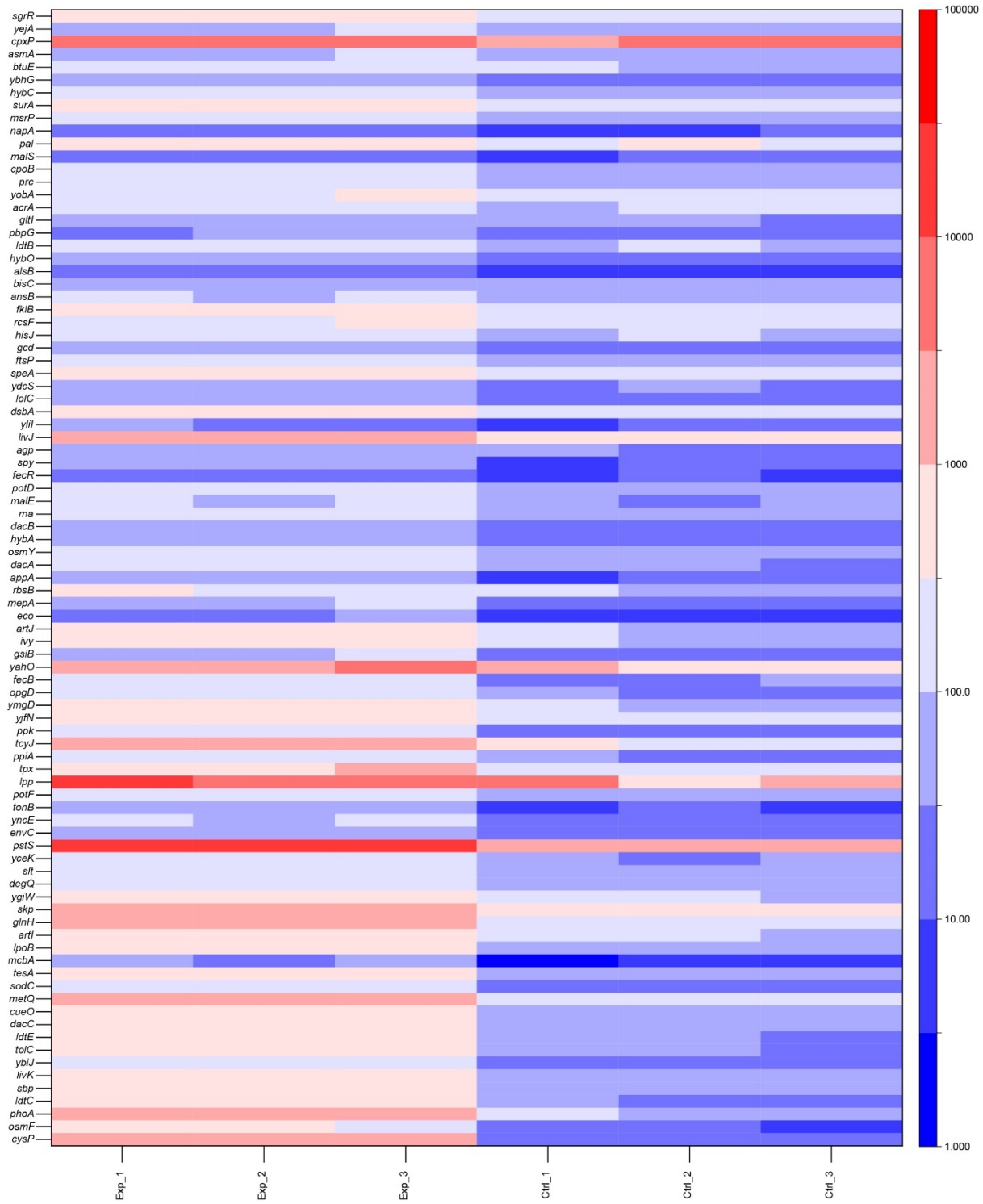

Fig. S23. Heatmap illustrating the up-regulation of genes encoding proteins located in the periplasmic space. The data indicate that the synthesis of CdS nanoclusters in the periplasmic space may also upregulate protein expression in the periplasmic space.

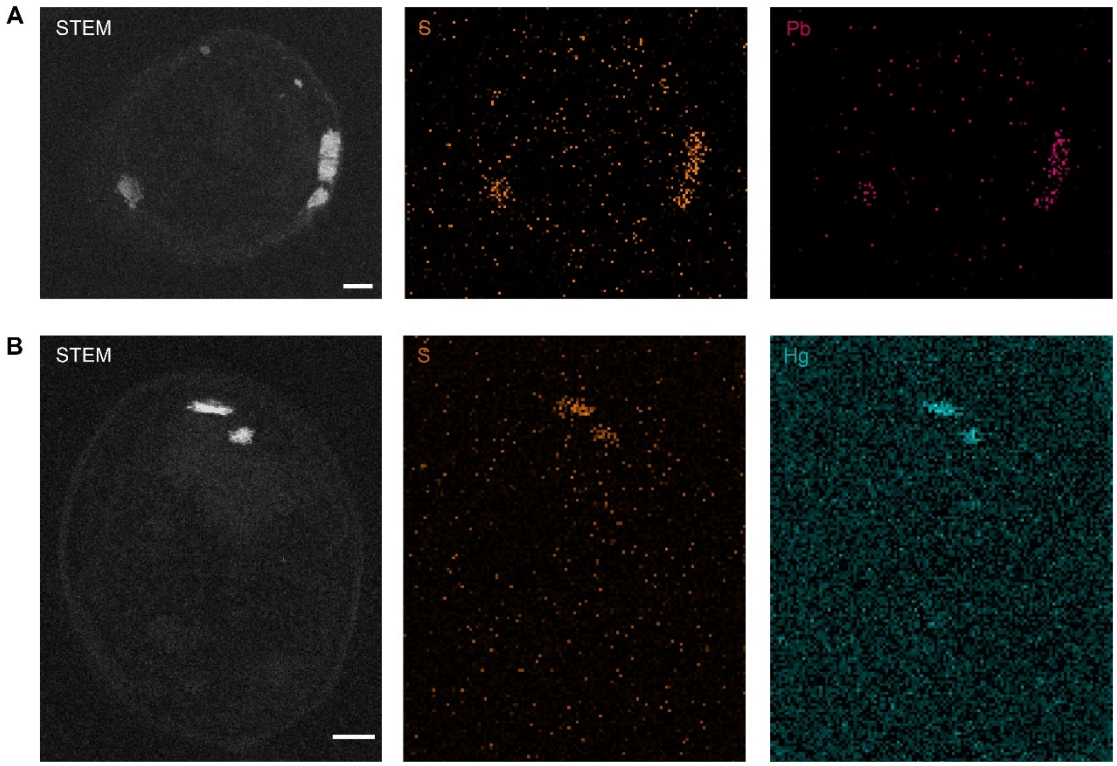

Fig. S24. STEM images and energy dispersive spectroscopy mapping of bacterial hybrids with biomineralized PbS or HgS nanoclusters. A) STEM-EDS mapping of biohybrids shows biomineralized nanoclusters are composed of Pb and S elements. Scale bar, 100 nm. **B**) STEM-EDS mapping of biohybrids shows that the biomineralized nanoclusters are composed of Hg and S. Scale bar, 100 nm.

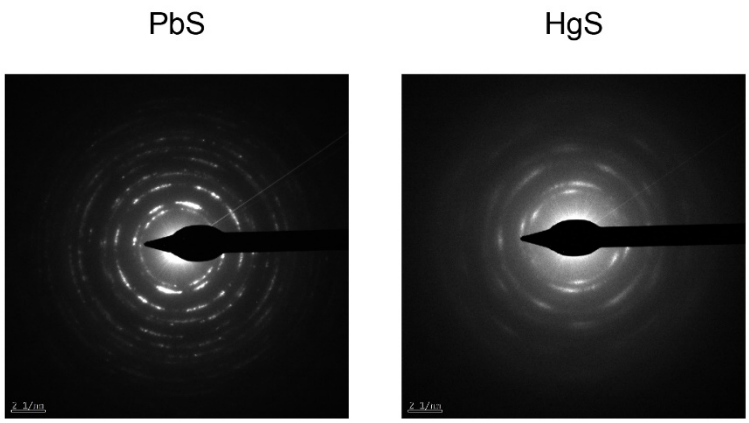

Fig. S25. Selected area electron diffraction (SAED) shows the crystallographic information for the PbS and HgS nanoclusters. PbS and HgS nanoclusters show well-defined crystalline structures.

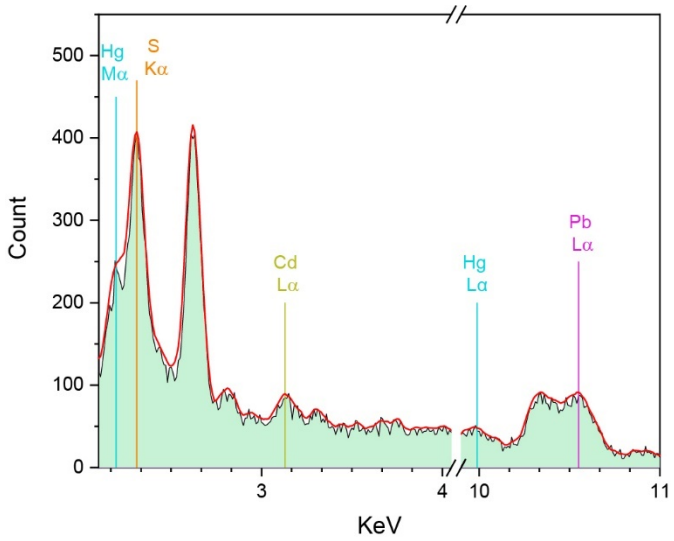

Fig. S26. EDS spectrum of the bacteria after multiplex biomineralization indicates the co-existence of CdS, PbS, and HgS.

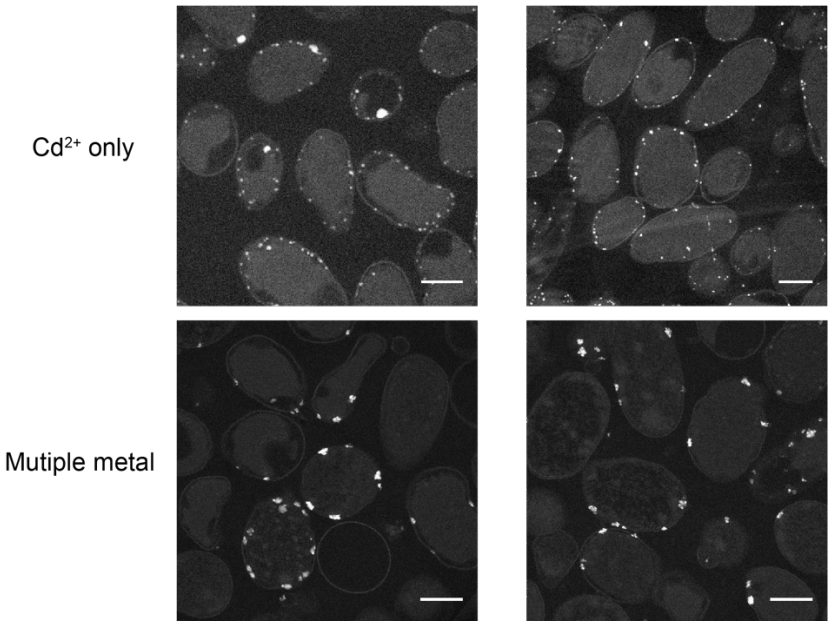

Fig. S27. Cross-sectional TEM images of *E. coil* cultured in Cd^{2+} alone and multiple metals (Cd^{2+}, Pb^{2+} and Hg^{2}) in the culture medium. Scale bar, 500 nm.

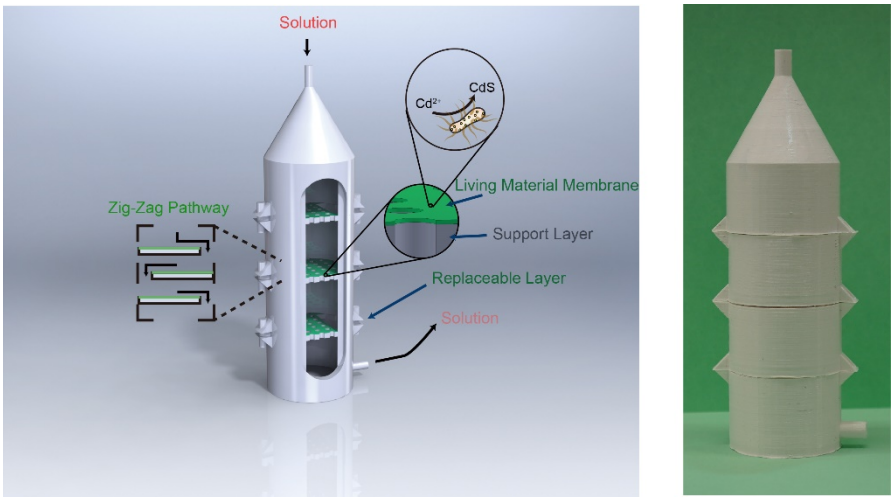

Fig. S28. Continuous bioprocessing reactor for biohybrids synthesis. The design of the reactor and the zoom-in images show the utilization of the living material membrane with a zig-zag pathway to induce biohybrids synthesis in a continuous manner. Left: Schematic; Right: a photograph of the actual reactor.

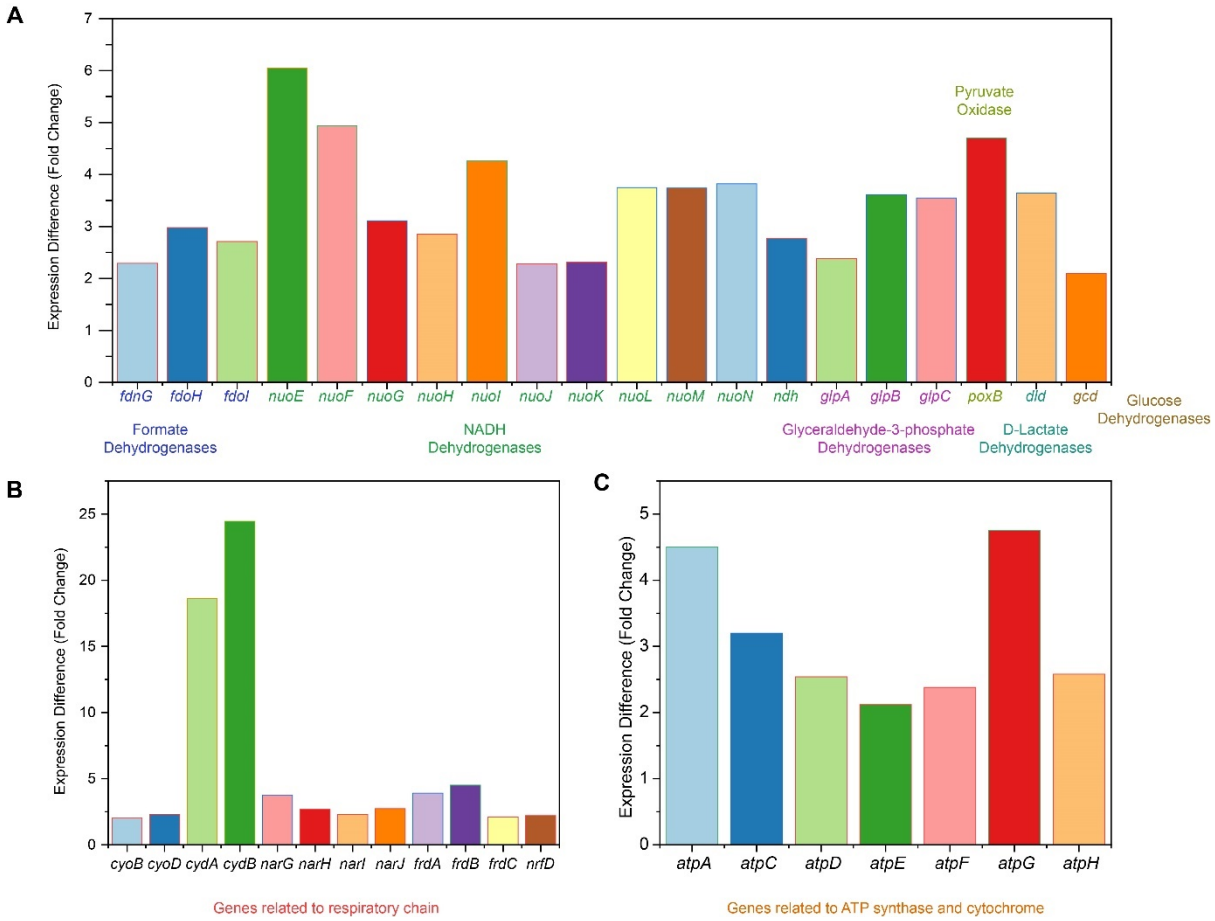

Fig. S29. Up-regulation of genes related to the respiratory electron transport chain. A) Multiple dehydrogenases-related genes, including formate dehydrogenases (*fdnG* (+2.29), *fdoH* (+2.98), *fdoI* (+2.71)), NADH dehydrogenases (*nuoE* (+6.05), *nuoF* (+4.94), *nuoG* (+3.11), *nuoH* (+2.85), *nuoI* (+4.26), *nuoJ* (+2.28), *nuoK* (+2.31), *nuoL* (+3.75), *nuoM* (+3.74), *nuoN* (+3.82), *ndh* (+2.77)), glyceraldehyde-3-phosphate dehydrogenases (*glpA* (+2.38), *glpB* (+3.61), *glpC* (+3.55)), pyruvate oxidase (*poxB* (+4.70)), D-lactate dehydrogenase (*dld* (+3.64)), glucose dehydrogenase (*gcd* (+2.10)), were up-regulated in Cd^{2+} and cysteine treated *E. coli* cells compared to those treated with Cd^{2+} only, suggesting an accelerated electron transport in the respiratory chain. **B**) Multiple terminal reductases and oxidases-related genes, including *cyoB* (+2.02), *cyoD* (+2.29), *cydA* (+18.62), *cydB* (+24.46), *narG* (+3.77), *narH* (+2.68), *narI* (+2.32), *narJ* (+2.74), *frdA* (+3.91), *frdB* (+4.51), *frdC* (+2.09), *nrfD* (+2.21), were up-regulated in Cd^{2+} and cysteine treated *E. coli* cells compared to those treated with Cd^{2+} only, suggesting an accelerated electron transport in the respiratory chain. **C**) Multiple ATP synthase-related genes, including *atpA* (+4.50), *atpC* (+3.20), *atpD* (+2.54), *atpE* (+2.12), *atpF* (+2.38), *atpG* (+4.75), *atpH* (+2.58), were up-regulated in Cd^{2+} and cysteine treated *E. coli* cells compared to those treated with Cd^{2+} only, suggesting the increased production of ATP during CdS nanoparticle and fimbriae formation.

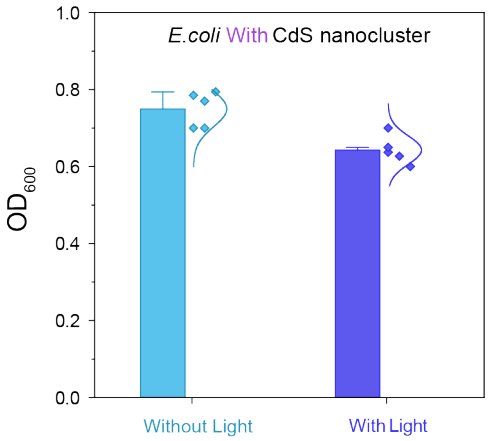

Fig. S30. The flask cultures with/without light stimulation have similar biomass. The OD_{600} values of the bacterial culture are all in the range between 0.6 and 0.8 in the experiment. The sample with light stimulation produces a much higher malate even with slightly less biomass (lower OD value).

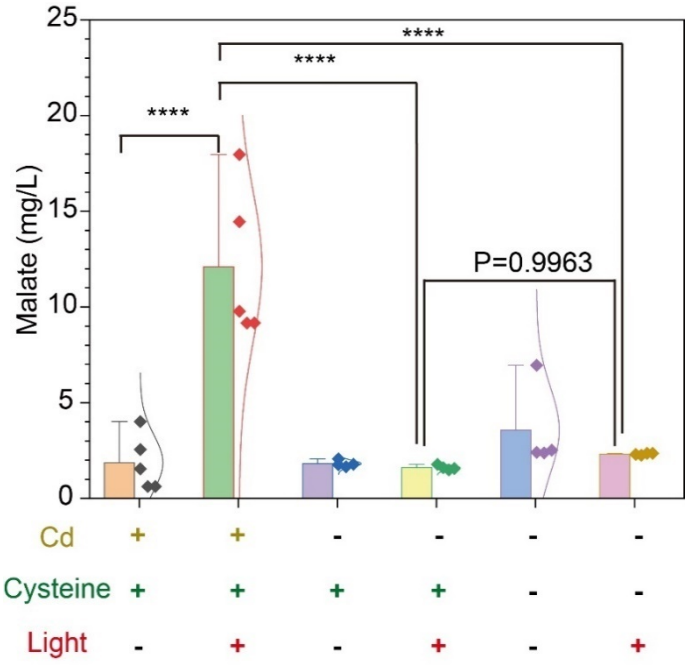

Fig. S31. Benchmark experiments showing the cysteine itself is not attributed to the notable enhancement in malate production.